www.czasopisma.pan.pl PAN www.journals.pan.pl
Archives of Acoustics Vol. **47**, No. 4, pp. 501–512 (2022), doi: 10.24425/aoa.2022.142894

Research Paper

Design of Sound Absorbers Based on Open-Cell Foams via Microstructure-Based Modeling

Van-Hai TRINH(1)*, Thien-Van NGUYEN(2), Thi-Hai-Nhu NGUYEN(3), Minh-Tan NGUYEN(1)

(1) *Faculty of Vehicle and Energy Engineering, Le Quy Don Technical University*
Ha Noi, Vietnam

(2) *Academy of Science and Technology*
Ha Noi, Vietnam

(3) *Faculty of Information Technology, Hanoi University of Civil Engineering*
Ha Noi, Vietnam

*Corresponding Author e-mail: hai.tv@lqdtu.edu.vn

(*received August 20, 2021; accepted June 30, 2022*)

Effects of microstructure factors on the acoustic performance of open-cell foams can be characterized numerically by a microstructure-based approach. To this regard, the numerical homogenization approach and the equivalent-fluid theory are employed to study the acoustic behavior of random open-cell foams within their Voronoi tessellation-based Representative Volume Elements (RVE). As a validation step, the numerical predictions are compared with the reference findings to either verify the finite element procedure or demonstrate that the constructed RVE can capture both the local geometrical characteristics and the acoustic macro-behavior of cellular solid foams. It can be seen from the obtained results that the morphological characteristics of open-cell foams could be controlled to achieve the desired sound absorbing behavior. In addition, the analytical expressions, formulating the relationship between the geometry of foam absorbers and their target absorption performance, are established to design sound absorbing foam layers.

Keywords: monodisperse foam; cellular morphology; transports; sound absorption; equivalent fluid; multiscale simulation.

1. Introduction

Porous structures and materials have recently served a wide application due to their high sound absorption and exhibiting other relevant features (e.g. weight, thickness, safety, recyclability). When the air propagates through a porous medium (i.e. foam, fibrous, granular), its freely traveling sound energy can be partially absorbed due to a combination of dissipation mechanisms including visco-inertial and thermal effects (Fahy, 2000; Allard, Atalla, 2009). The relationship between the microstructure parameters and the macroscopic behavior of sound absorbers can be predicted by different methods: (i) theoretical (Johnson et al., 1987; Champoux, Allard, 1991; Lagarge *et al.*, 1997; Allard, Atalla, 2009); (ii) experimental (Panneton, Olny, 2006; Olny, Panneton, 2008); and (iii) numerical one (Gasser *et al.*, 2005; Perrot *et al.*, 2007; Lee *et al.*, 2009; Nguyen *et al.*, 2022). These approaches allow to characterize and design the sound absorbing structures under various application constraints.

In open porous cellular structures, acoustic pressure in the pore connectivity vanishes mainly by the visco-inertial and thermal dissipations that dominate the sound absorbing performance rather than the visco-elastic frame effect. Consequently, the foam solid skeleton can be assumed rigid perfectly in modeling this class of sound absorbing materials (Fahy, 2000; Allard, Atalla, 2009; Dib *et al.*, 2015; Park *et al.*, 2017a). The macroscopic transport properties are influenced greatly by the cellular pore connections, thus a potential way to enhance their advanced functional performance (e.g. sound absorption) is tuning the local morphology foams (Doutres *et al.*, 2011; Trinh *et al.*, 2019; Langlois *et al.*, 2020; Jafari *et al.*, 2020).

The foamy morphology was fully characterized by experiments (Matzke, 1945; 1946) or simulations (Kraynik *et al.*, 2003; 2004; Köll, Hallström, 2014). In these studies, several morphology distributions (e.g. cell size, cell shape, face area, strut length) were considered. The findings stated clearly that: (i) the real foam has a very complex morphology that depends strongly on the manufacturing process; (ii) computational methods can successfully reconstruct this structure. In acoustic applications, it is observed that simple RVEs, e.g. mostly as tetrakaidecahedron shape (polyhedron with 14 faces) namely Kelvin cell, are widely used to study foam materials for both open (Perrot *et al.*, 2012; 2007) and semi-open cell (Doutres *et al.*, 2011; Gao *et al.*, 2016; Park *et al.*, 2017a) structures. The Weaire-Phelan structure, consisting of eight cells (two irregular dodecahedron and six like-tetrakaidecahedron), was proposed by Weaire and Phelan (1994). This equal-volume cell pattern could be a good candidate as an idealized unit cell for modeling and predicting foamy characteristics (Buffel *et al.*, 2014). For the case of foams having a wide distribution of pore size and shape, random RVEs can be required for characterization tasks of overall properties (Nguyen *et al.*, 2022).

In terms of the acoustic performance, the sound absorbing ability of foam-based absorbers is greatly influenced by their layer thickness (Chevillotte, Perrot, 2017) and local morphology features (porosity (Chevillotte, Perrot, 2017; Trinh *et al.*, 2018), cell size (Perrot *et al.*, 2012; Chevillotte, Perrot, 2017), level of membrane or solid film (Doutres *et al.*, 2013; Park *et al.*, 2017a; Trinh *et al.*, 2019), and polydispersity (Nguyen *et al.*, 2022)). It turns out that, as compared to the opened cell structures at a similar cell size scale, membrane foams having a reasonable reticulated level or controlled pore connection provide a higher sound absorption coefficient level (Park *et al.*, 2017b; Trinh *et al.*, 2019). However, manufacturing the design morphology of ultrathin membranes at scale of several micrometers, i.e. < 2 μm (Gao *et al.*, 2016; Trinh *et al.*, 2019) and keeping it during the use process still remains a challenge. It means that foams with and without membranes are both required to develop for their tuning sound absorbing properties, in which, great attention was paid to designing and optimizing the open-cell foam materials (Perrot *et al.*, 2008; 2012; Jafari *et al.*, 2020; Langlois *et al.*, 2020).

In addition, the issue related to the local morphology of open-cell foams and their acoustical behavior (e.g. transports, effective properties, and sound absorption) remains unanswered. Regarding this, the present work aims to develop a numerical framework for systematic predicting of the influence of the microstructure factors on the non-acoustical and acoustical parameters of open-cell foam absorbers.

This paper is organized as follows. Section 2 introduces the RVE reconstruction procedure. To generate the required ensemble of seed points, the method for randomly packing equal-sized spheres is first presented. Then, the polycrystalline structure of open-cell foam materials is reconstructed using the Voronoi tessellation. Section 3 briefly recalls the theoretical formulations describing the wave propagation phenomena in a pore connection. This summary focuses on hybrid-numerical approach using the multi-scale homogeneous technique and formulating a porous medium by the semi-phenomenological model. In Sec. 4, parametric analysis and design flowchart of the acoustic behavior of foam absorbers with varying structure parameters are demonstrated. Finally, some conclusions are drawn as well as forthcoming works are proposed.

2. Generation of microstructure representation

Figure 1 shows the microscopic presentation of a real foam structure whose pore connection is made of ligaments and vertices (also named struts and nodes). The reconstructed Voronoi-based model of the foam microstructure depends on the basic distribution of seed points (Kraynikm *et al.*, 2003; 2004; Kröll, Hallström, 2014). In this section, the morphology of monodisperse foams with open-cell structures is generated.

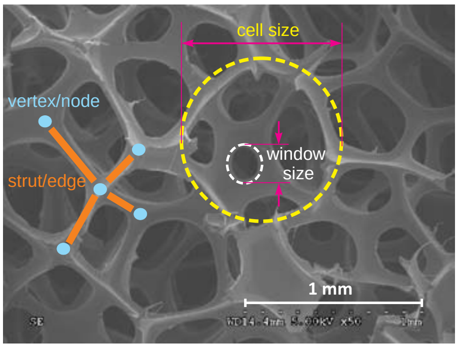

Fig. 1. Structure of a real monodisperse open-cell solid foam.

2.1. Dense random packing of rigid mono-sized spheres

Herein, we follow the popular algorithm provided by Jodrey and Tory (1981; 1985) to construct a randomly close-packed distribution of equal spheres. The method is briefly introduced in the following.

In the initial state, a set of N sphere centers is randomly distributed in a cubic unit. It is assumed that each generated point is the center of two spheres, namely the inner and the outer one with their corresponding diameter d_{in} and d_{out}.

The diameter $d_{\text{in}}^{(k)}$ is equal to the minimum center-center distance in the sphere ensemble as:

$$d_{\text{in}}^{(k)} = \min \left\| \mathbf{r}_{ij}^{(k)} := \mathbf{x}_i^{(k)} - \mathbf{x}_j^{(k)} \right\|, \quad i,j \in [1,N], \quad i \neq j. \tag{1}$$

In each step, two any overlapping spheres are separated by an equal distance along their center:

$$\mathcal{D}^{(k)} = \frac{1}{2}\frac{d_{\text{out}}^{(k+1)} - \left\|\mathbf{r}_{ij}^{(k)}\right\|}{\left\|\mathbf{r}_{ij}^{(k)}\right\|}. \tag{2}$$

The diameter $d_{\text{out}}^{(0)}$ is set initially to $(6/(\pi N))^{1/3}$ with a nominal volume faction of 1. If remaining overlaps, the diameter of the outer sphere is reduced slightly as follows (Jodrey, Torry, 1981; 1985):

$$\frac{d_{\text{out}}^{(k+1)}}{d_{\text{out}}^{(0)}} = \frac{d_{\text{out}}^{(k)}}{d_{\text{out}}^{(0)}} - \frac{\kappa_i}{2^{\Gamma} N}, \tag{3}$$

where κ_i is the initial rate of contraction, and $\Gamma = \lfloor -\log_{10}\Delta\eta_{\text{p}}^{(k)} \rfloor$ with $\lfloor . \rfloor$ is the greatest integer function. $\Delta\eta_{\text{p}}^{(k)}$ is the difference of the volume packing fraction between two sphere ensembles at iteration k, when $\Delta\eta_{\text{p}}^{(k)} \le 0$ the packing algorithm is terminated.

To address the periodic conditions for the RVE skeleton, a technique introduced in (Ghossein, Levesque, 2012) can be used. This tool generates periodic particles according to collisions of a sphere with the cubic faces. For each intersect collision, the location of the periodic sphere ${}^{p}\mathbf{x}_i$ is defined from the location $\mathbf{x}_i$ of its original sphere as ${}^{p}\mathbf{x}_i = \mathbf{x}_i + \mathbf{h}$, in which the number of periodic spheres p and the components of the offset vector $\mathbf{h} = [h_i]_{1\times 3}$ depend on the location of the intersect face, i.e. $p \in \{-1;\ 3;\ 7\}$ and $h_i \in \{-1;\ 0;\ 1\}$.

For representation purposes, Fig. 2 shows an assembly of 1024 spheres with a volume fraction of 0.60 and the corresponding radial distribution function $g(r)$ compared to several loose packing configurations (i.e. $\eta_p < 0.60$). This ensemble was generated in around 1100 seconds on an Intel(R) Core(TM) i7-4500U, CPU@ 1.80 GHz 2.40 GHz, and 4 GB RAM. The algorithm may require a much lower number of iterations for non-periodic packings.

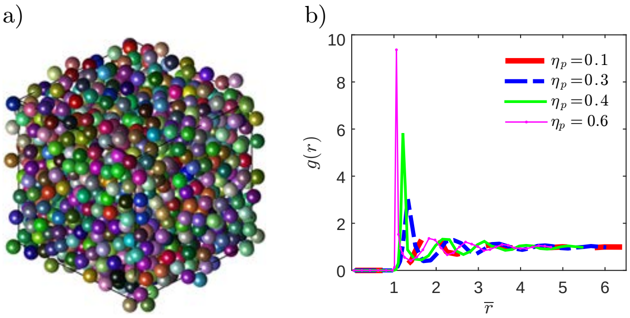

Fig. 2. a) Random close packed ensemble of 1024 mono-sized spheres with a packing density of $\eta_p = 0.60$; b) graph $g(r) \to \overline{r}(= 2r/d)$ for different packing fractions.

2.2. Foam microstructure generation

The Voronoi pattern-based cell system is developed from the set of seeds or nucleus generated in Subsec. 2.1. The Voronoi cell V_i corresponding to the point $P_i(\mathbf{x}_i)$ is defined as the space domain of $\mathbf{x}$ closer to that seed than any other seeds $P_j(\mathbf{x}_j)$ (Okabe, 1992):

$$V_i(\mathbf{x}_i) = \{\mathbf{x} \in \mathbb{R}^3 \mid \ \|\mathbf{x} - \mathbf{x}_i\| \le \|\mathbf{x} - \mathbf{x}_j\|, \text{ for all } j \neq i\}. \tag{4}$$

The Voronoi diagram is constructed from all single Voronoi cells which is a union of convex polyhedrons without any overlaps. As an illustration, the 3D Voronoi diagram shown in Fig. 3b corresponds to the random dense packing of spheres in Fig. 3a. In this structure, the cell edges and vertices present the ligaments and the nodes of the foam morphology, respectively. In membrane foams, it was noticed that the cell walls or faces with a given thin membrane should be used for modeling the foams with solid films that close fully or partially the pore connection. From the Voronoi diagram, an established RVE skeleton of the foam within cylindrical struts is provided in Fig. 3c, and the finite mesh model of its fluid phase shown in Fig. 3d can be used for multiscale simulations in the next section.

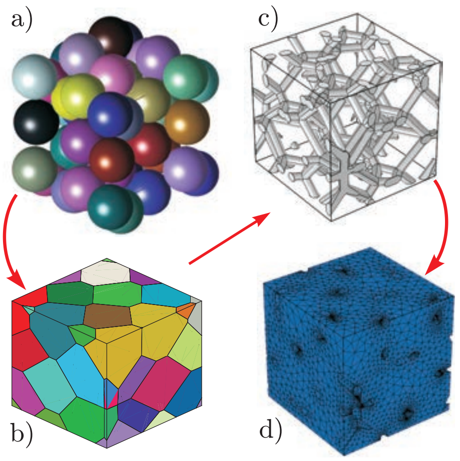

Fig. 3. Steps in the foamy structure generating: a) dense packing of spheres; b) periodic pattern based on Voronoi cells; c) representative element volume of solid foams; d) FE mesh of pore domain containing 218 811 tetrahedral elements.

It was noticed that the regular structures (e.g. Kelvin or Weaire-Phelan pattern) can be created from an appropriate set of ordered seed points, i.e. the body-centered cubic lattice or the lattice with the seed coordinates shown in Fig. 2 in (Weaire, Phelan, 1994).

For the random RVE model, the average cell size in the foam ensemble is estimated through the mean cell volume $\overline{V}_{ce}$ as:

$$\overline{C}_s = \left(6\frac{\overline{V}_{ce}}{\pi N_c}\right)^{1/3}, \tag{5}$$

where $\overline{V}_{ce} = 1/N_c \sum_{i=1}^{N_c} V_{cei}$ with V_{cei} is volume of the i-th cell in the ensemble of N_c cells.

Based on the RVE, two geometrical factors of the pore connection of foams, namely, the open porosity ϕ and the thermal characteristic length Λ', can be estimated by:

$$\phi = \frac{\iiint\limits_{\Omega_f} \mathrm{d}V}{\iiint\limits_{\Omega} \mathrm{d}V}, \qquad \Lambda' = 2\frac{\iiint\limits_{\Omega_f} \mathrm{d}V}{\iint\limits_{\partial\Omega_f} \mathrm{d}S}, \tag{6}$$

where Ω_f and $\partial\Omega_f$ denote respectively the fluid domain and the solid-fluid interface of the RVE domain Ω.

3. Computations of transport and acoustic properties

Acoustic porous layers can be formulated by two frequency-dependent properties (i.e. effective density and bulk modulus). This description includes two geometrical factors (ϕ, Λ') and six macroscopic transports involving (i) four factors regarding the viscous-internal effects and (ii) two factors regarding the thermal effects. From these effective representations, the sound absorbing coefficient of absorbers can be estimated. We herein present the computational scheme for this modeling framework.

3.1. Hybrid multiscale calculations

Below is a brief introduction about the first principles for estimations of the above transports.

3.1.1. Stokes problem

At the low-frequency limit (that is, $\omega \to 0$), Stokes or viscous flow in interconnected pores of the foams can be governed by the following equations and boundary conditions (Auriault *et al.*, 2010):

$$\eta\Delta\mathbf{v} - \nabla p = -\mathbf{G} \quad \text{with} \quad \nabla\cdot\mathbf{v} = 0 \quad \text{in} \quad \Omega_f, \tag{7}$$

with $\mathbf{v} = 0$ on $\partial\Omega_f$, and $\mathbf{v}$, p are Ω-periodic; η, $\mathbf{v}$, and p are the dynamic viscosity, velocity, and pressure of the fluid, respectively; $\mathbf{G}$ is the imposed macroscopic pressure gradient. Symbols Δ and ∇ denote the Laplacian and nabla operators.

The components of two static viscous factors, the permeability tensor $\mathbf{k}_0 = [k_{0ij}]_{3\times3}$ and the tortuosity tensor $\boldsymbol{\alpha}_0 = [\alpha_{0ij}]_{3\times3}$, are calculated as (Boutin, Geindreau, 2008):

$$k_{0ij} = \phi\left\langle k^{\star}_{0ij}\right\rangle, \qquad \alpha_{0ij} = \frac{\left\langle k^{\star}_{0pi}k^{\star}_{0pj}\right\rangle}{\left\langle k^{\star}_{0ii}\right\rangle\left\langle k^{\star}_{0jj}\right\rangle}, \tag{8}$$

wherein $k^{\star}_0$ is the local static viscous permeability as $\mathbf{v} = -(1/\eta)k^{\star}_0\mathbf{G}$, and $\langle\bullet\rangle = (1/|\,\Omega_f\,|)\iiint\limits_{\Omega_f}\bullet\,\mathrm{d}V$.

In general, by solving Eq. (7) we can define a set of all nine components of each transport tensors. For the case of permeability, its coefficients can be deduced from three separate procedures with the corresponding imposed gradient $\mathbf{G}$ (e.g. $\mathbf{G}_x = [1 \;\; 0 \;\; 0]^{\mathrm{T}}$ is for estimations of components $[k_{0xx} \; k_{0yx} \; k_{0zx}]^{\mathrm{T}}$). However, referring to a geometry symmetry, the second order macroscopic transport tensors become a diagonal form (i.e. $\mathbf{k}_0 = k_0\mathbf{I}_3$ and $\boldsymbol{\alpha}_0 = \alpha_0\mathbf{I}_3$ with $\mathbf{I}_3$ is the identity matrix).

3.1.2. Laplace problem

When $\omega \to +\infty$ (i.e. high-frequency regime), the inertial flow in a pore domain behaves like an ideal fluid (i.e. no viscosity), thus its governing formulation has the same form as the equations of the electric conduction phenomenon (Johnson *et al.*, 1987; Avellaneda, Torquato, 1991; Achdou, Avellaneda, 1992). Therefore, the macroscopic properties of interest can be computed from the following equations known as the Laplace problem:

$$\mathbf{E} = -\nabla\varphi + \mathbf{e} \quad \text{with} \quad \nabla\cdot\mathbf{E} = 0 \quad \text{in} \quad \Omega_f, \tag{9}$$

with $\mathbf{E}\cdot\mathbf{n} = 0$ on $\partial\Omega_f$, and φ is Ω-periodic. Herein, $\mathbf{E}$ is the electric field, φ is an electric potential, $\mathbf{e}$ is a given unit vector field, and $\mathbf{n}$ is the unit vector normal to $\partial\Omega_f$.

Within symmetric properties, the high-frequency tortuosity tensor $\boldsymbol{\alpha}_\infty = [\alpha_{\infty ij}]_{3\times3}$ and the viscous characteristic length tensor $\boldsymbol{\Lambda} = [\Lambda_{ij}]_{3\times3}$ can be described by a scalar calculated as (Johnson *et al.*, 1987; Lafarge, 2099):

$$\boldsymbol{\alpha}_\infty = \frac{\left\langle\mathbf{E}^2\right\rangle}{\left\langle\mathbf{E}\right\rangle^2}, \qquad \boldsymbol{\Lambda} = 2\frac{\iiint\limits_{\Omega_f}\mathbf{E}^2\,\mathrm{d}V}{\iint\limits_{\partial\Omega_f}\mathbf{E}^2\,\mathrm{d}S}. \tag{10}$$

3.1.3. Poisson problem

When $\omega \to 0$, heat diffusion in the pore phase is formulated as (Rubinstein, Torquato, 1988):

$$\nabla^2 u = -1 \quad \text{in} \quad \Omega_f, \tag{11}$$

with $u = 0$ on the fluid-solid interface $\partial\Omega_f$ and u is Ω-periodic.

The local solution u is used for calculating two remaining macroscopic transports as (Avellaneda, Torquato, 1991):

$$k'_0 = \langle u\rangle, \qquad \alpha'_0 = \frac{\left\langle u^2\right\rangle}{\langle u\rangle^2}, \tag{12}$$

where k_0' is the static thermal permeability and α_0' is the static thermal tortuosity.

From the local field solutions of three above-described static problems, see Fig. 4 for instance, we can deduce the corresponding transport parameters as input factors of the semi-phenomenological model presented in the next section.

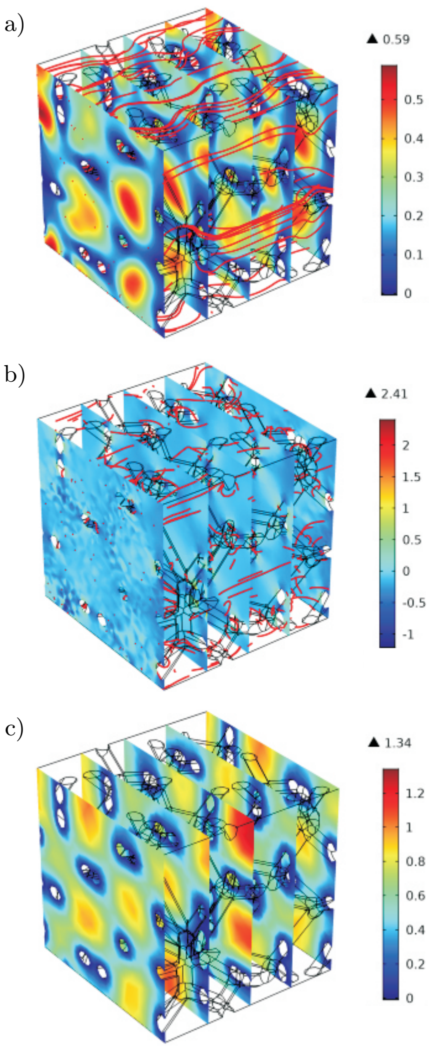

Fig. 4. Graphs of three local asymptotic fields: a) k^*_{0xx} ($\times 10^{-8}$ m^2) with an imposed unit $\mathbf{G}_x$; b) $E_{xx}/\nabla\varphi$ (–) with an imposed unit field $\mathbf{e}_x$; c) u ($\times 10^{-8}$ m^2).

3.2. Acoustic model of porous media

In the equivalent-fluid theory (Lafarge, 2009; Allard, Atalla, 2009), the air in a porous structure (i.e. pore phase) might be replaced by an equivalent fluid with its macroscopic representation (i.e. two frequency-dependent properties). In the Johnson-Champoux-Allard-Pride-Lafarge (JCAPL) or eight-parameter semi-phenomenological model, the frequency-dependent density $\widetilde{\rho}(\omega)$ and the frequency-dependent bulk modulus $\widetilde{K}(\omega)$ are estimated from the transport properties governing the viscous-internal and thermal effects as follows (Johnson *et al.*, 1987; Champoux, Allard, 1991; Lafarge *et al.*, 1997):

$$\widetilde{\rho}(\omega) = \frac{\rho_0\alpha_\infty}{\phi}\left[1 + \frac{\eta\phi}{j\rho_0 k_0\alpha_\infty\omega} \cdot \left(1 - P + P\sqrt{1 + j\frac{M}{2P^2}\frac{\alpha_\infty\rho_0 k_0\omega}{\eta\phi}}\right)\right], \qquad (13)_1$$

and

$$\widetilde{K}(\omega) = \frac{\gamma P_0}{\phi}\left[\gamma - (\gamma-1)\left(1 + \frac{\eta\phi}{jk_0' N_{pr}\rho_0\omega} \cdot \left(1 - P' + P'\sqrt{1 + j\frac{M'}{2P'^2}\frac{k_0' N_{pr}\rho_0\omega}{\eta\phi}}\right)\right)^{-1}\right]^{-1}, \qquad (13)_2$$

with

$$M = \frac{8k_0\alpha_\infty}{\Lambda^2\phi}, \qquad M' = \frac{8k_0'}{\Lambda'^2\phi},$$
$$P = \frac{M}{4(\alpha_0/\alpha_\infty - 1)}, \qquad P' = \frac{M'}{4(\alpha_0' - 1)}. \qquad (14)$$

In above equations, ρ_0 is the air density at rest, γ is the ratio of heat capacity, P_0 is the atmospheric pressure, N_{pr} is the Prandtl number, and $\omega = 2\pi f$ is the angular frequency.

The sound absorption coefficient at normal incidence of a rigid-backed absorber is finally defined by:

$$A_\alpha(\omega) = 1 - \left|\frac{\widetilde{Z}_s(\omega) - \rho_0 c_0}{\widetilde{Z}_s(\omega) + \rho_0 c_0}\right|^2, \qquad (15)$$

with

$$\widetilde{Z}_s(\omega) = -j\sqrt{\widetilde{\rho}(\omega)\widetilde{K}(\omega)}\cot\frac{\omega L}{\sqrt{\widetilde{K}(\omega)/\widetilde{\rho}(\omega)}}, \qquad (16)$$

where L is the absorber thickness and c_0 is the sound speed in air.

4. Results and discussion

4.1. Foamy morphology

Using the procedure described in Sec. 2, some morphology characteristics of random monodisperse foams are discussed in this section. The obtained characteristics of the generated structures are compared with both the experimental characterization data (Matzke, 1946) and computational results (Kraynik *et al.*, 2003; Köll, Hallström, 2014) previously reported. Figure 5 shows the distribution of face number per cell $\mathcal{P}(F)$ (see the left panel) and the distribution of edge number per face $\mathcal{P}(E)$ (see the right panel). The cell

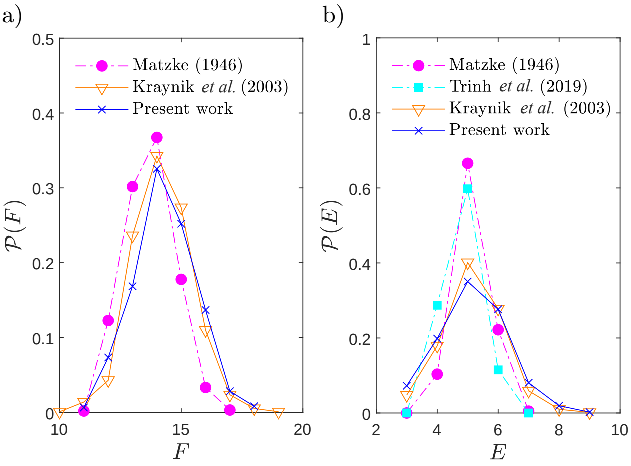

Fig. 5. Distributions of (a) F-face cells and (b) E-edge faces in foam structures.

volume V_{ce} and the strut length L_{li} are respectively normalized by $\widetilde{V}_{ce} = V_{ce}/\overline{V}_{ce}$ and $\widetilde{L}_{li} = L_{li}/\overline{L}_{li}$, in which the mean length $\overline{L}_{li}$ is estimated from the average cell volume $\overline{V}_{ce}$ as $\overline{L}_{li} = \overline{V}_{ce}^{1/3}$. Two observed distributions $\widetilde{V}_{ce} \mapsto \mathcal{P}(\widetilde{V}_{ce})$ and $\widetilde{L}_{li} \mapsto \mathcal{P}(\widetilde{L}_{li})$ are graphed in Fig. 6. The numerical results compare well with the reference works, and the virtual foam structure captures well some key morphology features such as (i) the 14-face cells (Fig. 5a) and the 5-sided faces (Fig. 5b) are the most frequent in the foam ensemble, and (ii) the monodispersity corresponds to a narrow distribution of the normalized cell volume (see Fig. 6a).

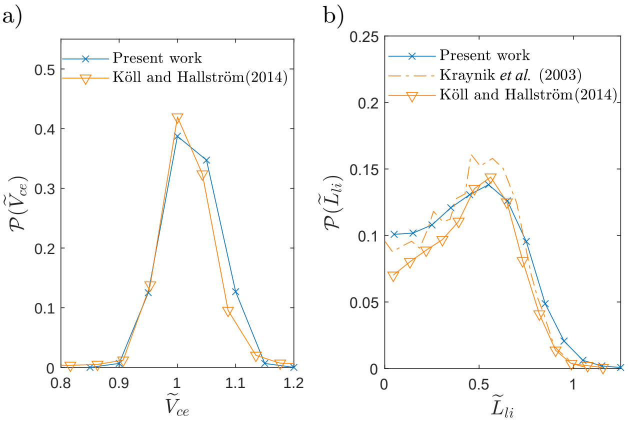

Fig. 6. Graphs of the normalized cell volume (a) and the normalized edge length (b) distributions of Voronoi random foam as compared with previous numerical works.

Regarding the structure that has narrow distributions, $\mathcal{P}(E)$ and $\mathcal{P}(\widetilde{L}_{li})$, a relaxation step could be required (Kraynik *et al.*, 2003; Köll, Hallström, 2014) in Surface Evolver (Brakke, 1992). After this step, the relaxed structure foam can be generated. In this structure, the proportion of the cell windows in pentagon shape is larger than 60% as found in the Matzke experimental data (see Fig. 5b). It was noticed that this statement is also confirmed in foams with a tuned membrane level (Trinh *et al.*, 2019).

4.2. Transport and effective properties of foams

In this part, the macroscopic transport properties and the effective factors of open-cell foam structure are studied. Figures 7–9 depict the results of the pro-

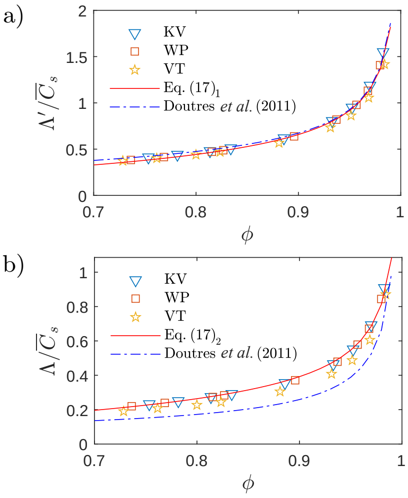

Fig. 7. Effect of microstructure (i.e. $\overline{C}_s$, ϕ) on the thermal (a) and viscous (b) characteristic lengths. Numerical estimations are shown with Kevin pattern (KV, ▽), Waire-Phelan pattern (WP, □), and Voroinoi tessellation (VT, ⋆). The continuous lines are the fitting curves from Eq. (17). Dashed lines in sub-figures (a, b) denote the analytical models proposed by Doutres *et al.*, (2011).

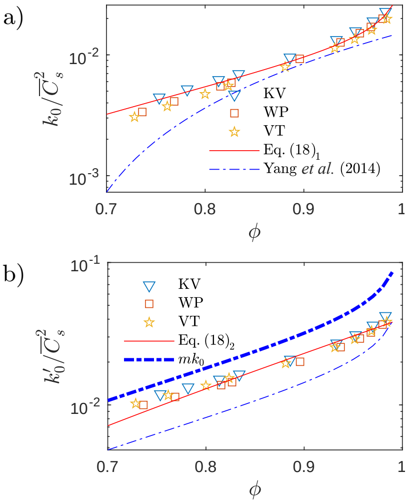

Fig. 8. Effect of microstructure on the viscous (a) and thermal (b) static permeabilities. Numerical estimations are shown with Kevin pattern (KV, ▽), Waire-Phelan pattern (WP, □), and Voronoi tessellation (VT, ⋆). Continuous lines are the fitting curves from Eq. (18) and the dashed line in sub-figures (a) denotes the analytical models proposed by Yang *et al.* (2014). For k_0' in panel (b), the dashed thin and thick lines are plotted with a ratio k_0'/k_0 equal to 3/2 and 10/3 as mentioned in (Vu *et al.*, 2019; Lafarge, 1993).

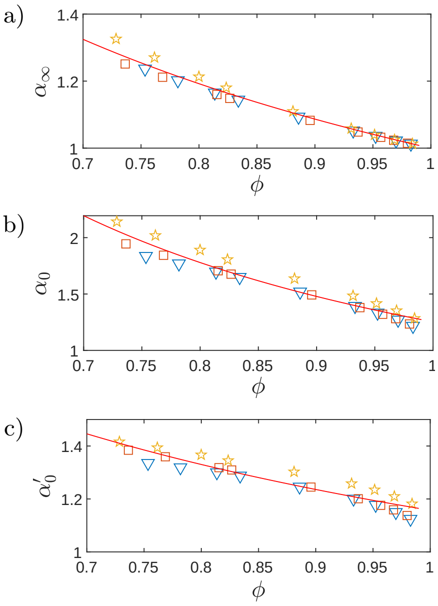

Fig. 9. Porosity-tortuosity relations of open-cell foams: high-frequency tortousity (top), static viscous tortuosity (middle), and static thermal tortuosity (bottom). Numerical estimations are shown with Kevin pattern (▽), Waire-Phelan pattern (□), and Voronoi tessellation (⋆). The continuous lines are the fitting curves from Eq. (19).

posed multiscale computations in comparison with the several analytical models for the characteristic lengths, permeabilities, and tortuosities, respectively.

It is seen that the RVEs based on different polyhedron patterns (including Kevin pattern, Waire-Phelan pattern, and Voronoi tessellation) can consistently predict the foamy transports. From these numerical values (in a porosity range of $0.70 \leq \phi \leq 0.99$ (Chevillotte, Perrot, 2017), several microstructure-transport relationships are generated. The following equations are for two characteristic lengths:

$$\frac{\Lambda'}{\overline{C}_s} = a_1 \frac{\phi}{(1-\phi)^{a_2}}, \qquad \mathbf{\Lambda} = \Lambda'/n, \tag{17}$$

with $a_1 = 0.2901$, $a_2 = 0.4010$, and $n = 1.677$.

Equation $(17)_1$ is developed from the definition of the thermal characteristic length as $\Lambda' = 2\phi/S_p$ (Perrot *et al.*, 2012) with the specific area of the fluid-solid surface S_p being a function of the solid fraction, $(1-\phi)$. Note that ratio n between two characteristic lengths in Eq. $(17)_2$ is nearly 1.55 for high porosity open-cell foams in (Doutres *et al.*, 2011), which also relies on the range [1, 2] found by Allard and Champoux (1992) for fibrous materials.

For permeability parameters, the viscous static permeability is assumed as function of $\phi^3/(1-\phi)^k$ (known as Kozeny–Carman equation (Costa, 2006)), whereas the thermal static one is related to two purely geometrical factors (ϕ, Λ') as $k'_0 \sim \phi\Lambda'^2/8$ (Lafarge *et al.*, 1997). That leads to the following expressions:

$$\frac{k_0}{\overline{C}_s^2} = b_1 \frac{\phi^3}{(1-\phi)^{b_2}}, \qquad \frac{k'_0}{\overline{C}_s^2} = c_1 \frac{\phi^3}{(1-\phi+c_2)^2}, \tag{18}$$

with $b_1 = 0.6491 \times 10^{-2}$, $b_2 = 0.3063$, $c_1 = 0.02359$, and $c_2 = 0.7646$.

Extending Archie's law in (Archie, 1942) to the multiscale estimations, the analytical approximations for three tortuosities are found as functions of the porosity:

$$\alpha_\infty = 1/\phi^{d_1}, \qquad \alpha_0 = 1.253/\phi^{d_2}, \qquad \alpha'_0 = 1.157/\phi^{d_3}, \tag{19}$$

in which $d_1 = 0.7882$, $d_2 = 1.571$, and $d_3 = 0.6252$. These observed porosity-tortuosity equations accord with the theoretical constraints proposed by Lafarge (2009) in the valid range of porosity: (i) $\alpha_0/\alpha_\infty > 1$ (i.e. $1.253/\phi^{(d_2-d_1)} > 1.26$); (ii) $\alpha_0/(\alpha_\infty\alpha'_0) > 1$ (i.e. $1.083/\phi^{(d_2-d_1-d_3)} > 1.02$), and $\alpha'_0 > 1$.

Next, the proposed method is validated with a reference to porous configuration based on the classical face-centered cubic (FCC) lattice with a porosity of $\phi = 0.26$. The sphere radius is equal to 1 mm, and their necks (at the contact points) have a radius of 0.15 mm (Gasser *et al.*, 2005). Figure 10 compares the effective properties of the FCC lattice from the present estimations (dashed line) and the reference values (markers) adopted from Gasser *et al.* (2005). Two computational schemes show a good agreement, which validates greatly the proposed finite element modeling. As listed in Table 1, the comparison of the predicted transports for this reference FCC lattice also supports this statement.

As shown in Fig. 10, the normalized effective properties of open-cell foams (within $\overline{C}_s \in [0.02,\ 1]$ mm and $\phi = 0.98$) are compared with the FCC granular medium with the frequency range of $[1,\ 10^4]$ Hz. The observed curves reveal that: (i) the foam connectivity and the granular packing provide the different effective properties (see the real parts in Figs 10a and 10b); and (ii) these complex factors of open-cell foams are greatly influenced by their average cell size $\overline{C}_s$. In addition, within $\overline{C}_s \in [0.3,\ 0.5]$ mm as the same pore scale of the FCC lattice (sphere radius: 1 mm; contact neck radius: 0.15 mm), the imaginary part of both properties varies in the same range (see, Figs 10c and 10d). In the next section, the sound absorption performance of these porous media will be investigated.

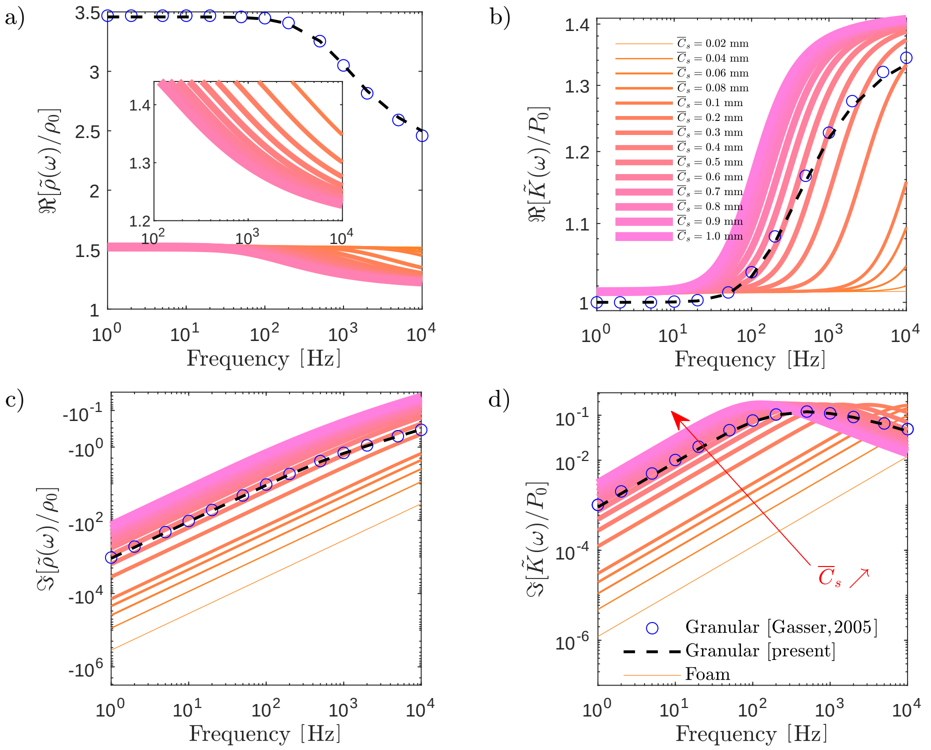

Fig. 10. Normalized values of $\widetilde{\rho}(\omega)$ (a, c) and $\widetilde{K}(\omega)$ (b, d) of open-cell foams (continuous lines, the thicker line the bigger cell size) are compared with that of the FCC granular medium (markers for reference data from Gasser *et al.* (2005) and dashed line for the present work, in which these effective properties are estimated using JCAPL model with the calculated factors presented in Table 1). Logarithmic scales are used for two bottom panels (i.e. imaginary parts).

Table 1. Computed transport properties in comparison with the reference estimations for two porous layers: FCC packing (Lee *et al.*, 2009) and melamine foam structure (Lai *et al.*, 2000).

Reference	Macroscopic transport parameters							
	ϕ [–]	Λ' [mm]	Λ [mm]	k_0 [$\times 10^{-10}$ m^2]	k_0' [$\times 10^{-10}$ m^2]	α_∞ [–]	α_0 [–]	α_0' [–]
Lee *et al.*, 2009	0.26	0.247	0.159	6.70	27.0	1.65	2.49	1.85
Present		0.247	0.157	6.76	26.3	1.66	2.65	1.91
Lai *et al.*, 2000	0.99	0.30	0.10	13.0	NA	1.02	NA	NA
Present		0.41	0.24		19.2	1.01	1.27	1.16

4.3. Sound absorption of foam-based layers

The established analytical laws of the non-dimensional transports in Subsec. 4.2 are used to predict and design the sound absorbing coefficient of absorbers based on monodisperse open-cell foams. We herein tune two microstructure parameters (i.e. ϕ and $\overline{C}_s$) and the layer thickness L.

We validate the analytical expressions of macroscopic factors by a real melamine foam proposed in (Lai *et al.*, 2000) with available measured data of some transports and the sound absorption. For comparison, the average cell size of this foam is estimated using Eq. $(18)_1$ with an equivalent permeability $k_0^{eq} = \eta/\sigma$, herein $\sigma = 14000$ Rayls/m is the static resistivity measured on the sample. From the value of $\overline{C}_s$ and ϕ, using the corresponding expression generated in Subsec. 4.2, the six remaining factors can be found (Table 1). As shown in Fig. 11, the predicted curve and the measurement data show a good agreement, which demonstrates the predictive performance of the established models of the macroscopic transport properties.

Figure 12 plots the effects of the averaging cell size $\overline{C}_s$ and the layer thickness L on the sound absorbing capacity of foams at a porosity $\phi = 0.98$. The thickness L in the top and bottom panels are respectively 30 mm and 90 mm. From the plotted curves, it is seen that we can select the value of $\overline{C}_s$ to reach the sound absorption level and tune the desired frequency. Absorbers with $L = 30$ mm and $\overline{C}_s$ in a range [0.2, 0.3] mm can provide $A_\alpha > 80\%$ at frequencies >3 kHz. For the thicker absorbers (i.e. $L = 90$ mm),

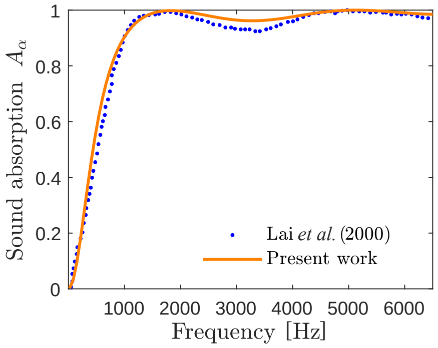

Fig. 11. Sound absorption of the melamine foam with $L = 51$ mm: solid dots (adopted from Lai *et al.* (2000)) and continuous line (the present work).

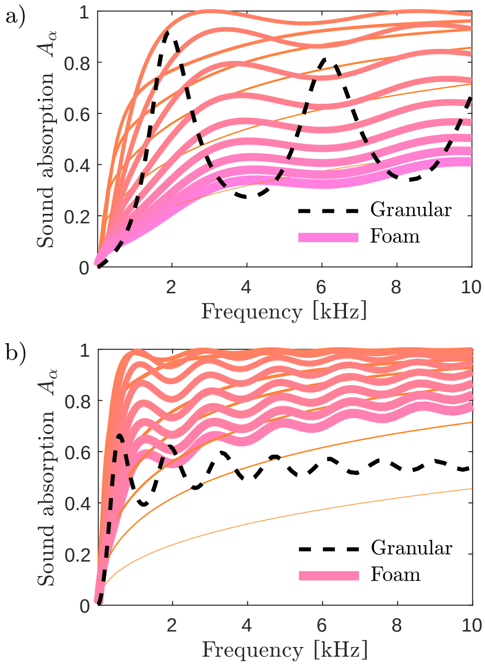

Fig. 12. Sound absorption of different porous absorbers with (a) $L = 30$ mm and (b) $L = 90$ mm. Foam layers have a tuned cell size (continuous lines as shown in Fig. 9, the thicker line for the larger cell size), whereas the granular layer is based on the FCC lattice (dashed lines) (Gasser *et al.*, 2005).

the sound absorption level of 80% can be achieved with $\overline{C}_s \in [0.2,\ 0.6]$ mm at low frequencies (> 1 kHz). In addition, within the smaller cell size (i.e. $[0.2,\ 0.4]$ mm, 90 mm thick layers of foams can be used for low frequency applications (~ 0.55 kHz) with a higher absorption level of 90%. The depicted curves also indicate that, compared with a FCC-based absorber with the same thickness, the foam layers have a smaller number of peaks and the first absorption peak occurs at a higher frequency for any values of $\overline{C}_s$. That can be generally caused by the relation of the complex wavelength of these porous media, $\Re(\lambda_{eq}^{\text{Foam}}) < \Re(\lambda_{eq}^{\text{FCC}})$ with $\lambda_{eq}(f) = f^{-1}\sqrt{\widetilde{K}(f)/\widetilde{\rho}(f)}$. In addition, the oscillation amplitude of quarter-wavelength resonance behavior decreases when reducing the cell size at a certain value (or high values of the dimensionless factor $L/\overline{C}_s$). The sound absorption curves reveal that we enable using the average cell size that provides the perfect absorption (i.e. $A_\alpha \approx 1$) at the first peak of the absorption behavior with a given thickness and porosity.

Then, we design foam absorbers for the desired sound absorption property. The question raised previously about the foam layers that produce the unit value of the absorption at the first peak with evidence as illustrated in Fig. 12. To address this target, we generate 9 classes of the foam absorbers having their thickness in the range $[20, 100]$ mm with a step of 10 mm. In each class, we design 5 foamy configurations corresponding to 5 values of different porosities (i.e. $\phi = 0.75/0.80/0.85/0.90/0.95/0.98$). Based on these configurations and the analytical expressions presented in Subsec. 4.2, we may find the value of $\overline{C}_s$ that provides the first peak with $A_\alpha = 1$. Figure 13 draws the findings for cases $\phi = 0.75$ and $\phi = 0.98$, respectively. With a smaller oscillation amplitude of quarter-wavelength resonance behavior, all curves for the case $\phi = 0.98$ show a better sound absorption (i.e. high sound absorption dips) compared with the lower porosity case.

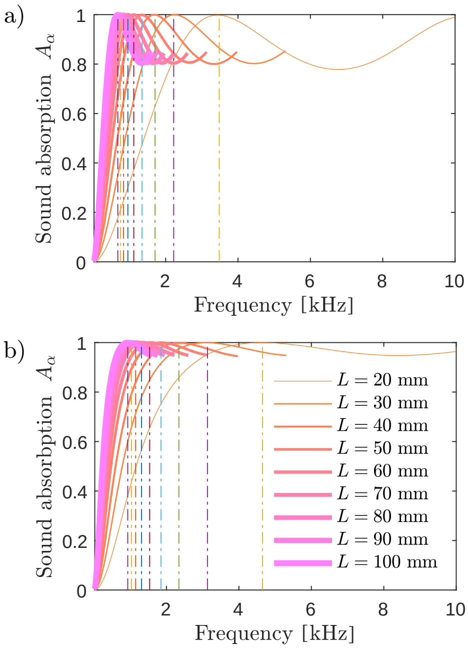

Fig. 13. Optimum sound absorbing coefficients of foam layers within their thickness varying from 20 mm (thinnest line) to 100 mm (thickest line): a) for $\phi = 0.75$ and b) for $\phi = 0.98$. For the sake of visibility, some values of A_α after the first peak are removed. The vertical dashed-dot lines refer to the first peak center.

For each pair of L_i and ϕ_i, we search a value of $\overline{C}_{si}$ that fulfills the sound absorption constraint $A_\alpha = 1$ at the first peak (i.e. f_{1i}). The found values of $(\overline{C}_{si},\ f_{1i})$ are depicted by circle markers in Figs 14 and 15. From these observations, the cell size-layer thickness and the first peak frequency-layer thickness relations are generated mathematically as follows:

$$\overline{C}_s = pL + q, \tag{20}$$

$$L = \delta / f_1. \tag{21}$$

In the expressions above, the average cell size $\overline{C}_s$ is in mm, the thickness layer L is in m, and the frequency of the first absorption peak f_1 is in Hz. The approximated coefficients $(p,\ q, \delta)$ are listed in Table 2, the values in each row present a given porosity.

Table 2. Fitting coefficients of Eqs (20) and (21).

Porosity ϕ	Coefficients		
	p	q	δ
0.75	5.500	0.3148	67.43
0.80	4.483	0.2932	71.06
0.85	4.007	0.2310	74.96
0.90	3.107	0.2074	79.99
0.95	2.890	0.1675	86.67
0.98	2.817	0.1232	92.58

From the optimal cell size-to-thickness ratio as shown in Fig. 14, it can be seen that (i) the thinner the optimal thickness the smaller cell size or the pore diameter, and this linear law is in accordance with the result proposed in (Vu *et al.*, 2019); (ii) the correlation between microstructure features (open porosity ϕ and cell size $\overline{C}_s$) and the layer thickness is consistent with the one studied by Chevillotte and Perrot (2017), in detail, for the high solid fraction foams, we need to control their pore size at a higher level compared with highly porous ones. In Eq. (21), for $\phi = 0.75$, the value $\delta = 67.43$ is nearly 61.36 for granular media based on random close packings of rigid spheres (Vu *et al.*, 2019), see Fig. 15.

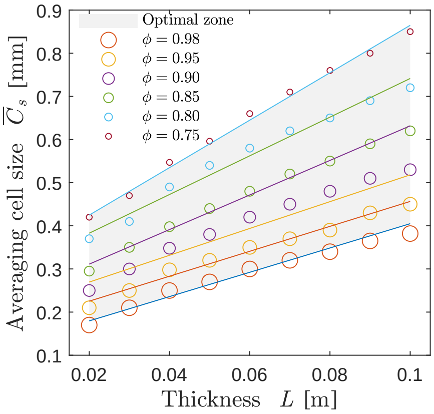

Fig. 14. Optimum average cell size for a given thickness of a foam absorber whose first peak has a total sound absorption (i.e. $A_\alpha = 1$). From top to bottom, the results are shown with an increase in porosity from 0.75 to 0.99 (as increasing the marker size). Markers are the considered points, and the lines are the fitting linear laws.

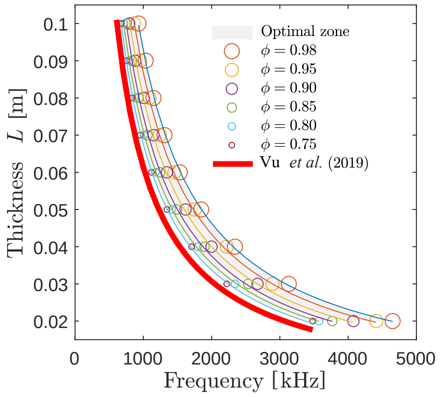

Fig. 15. Frequency at the first absorption peak of the optimal absorbers. Circle markers are the considered points, and the thin lines are the fitting exponential laws. The size of circle markers indicates an increase in the porosity of foams. The thick line presents the expression for sphere-packed media (Vu *et al.*, 2019).

From Eqs (20) and (21), an absorber owning 100% sound absorption at a given frequency can be designed by following several scenarios: (i) input f_1, one constraint factor and two remaining tuned factors in a set of $(L, \phi, \overline{C}_s)$; and (ii) input f_1, but two constraint factors and one remaining tuned factor. Three factors are tuned or constrained in the designing input space indicated by the gray zone in Figs 14 and 15. Note that within the constraint range of the open porosity, the low-frequency target (e.g. < 678 Hz) can be enhanced by using layer thicknesses > 0.1 m.

5. Conclusion

The effective absorption properties of open-cell foam materials were characterized systematically by a homogenization approach. Based on the numerical estimations of macroscopic transport properties, the effects of the average cell size and the porosity on the acoustic performance of foam layers have been studied. Through the present observations, the following concluding remarks can be drawn:

- Microstructure-based modeling is able to capture the foam morphology and generate the micro-macro relationships which are in accordance with results provided in the literature. The methodology serves as a computation scheme for systematic studying sound-absorbing foams.
- Under design and application constraints, the desired sound-absorbing property of foams with an open-cell structure can be achieved by adjusting the microstructure variables and the layer thickness.
- The semi-analytical relations, $L(f_1, \phi)$ and $\overline{C}_s(L, \phi)$ in Eqs (20) and (21), could be helpful for designing

foam absorbers with perfect sound absorption at desired frequencies within the design space.

Finally, it should be noted that without further developments, the proposed framework can be extended for: (i) considering the target as the average absorption over a specific band (e.g. low or high frequencies) or other functional property (e.g. sound transmission loss); (ii) including more morphology parameters such as polydisperse/graded foams.

Acknowledgments

This work is funded by the Vietnam National Foundation for Science and Technology Development (NAFOSTED) under Grant Number 107.01-2019.316.

References

1. Achdou Y., Avellaneda M. (1992), Influence of pore roughness and pore-size dispersion in estimating the permeability of a porous medium from electrical measurements, *Physics of Fluids A: Fluid Dynamics*, **4**(12): 2651–2673, doi: 10.1063/1.858523.
2. Allard J., Atalla N. (2009), *Propagation of Sound in Porous Media: Modelling Sound Absorbing Materials*, 2nd ed., John Wiley & Sons, Chichester.
3. Allard J.F., Champoux Y. (1992), New empirical equations for sound propagation in rigid frame fibrous materials, *The Journal of the Acoustical Society of America*, **91**(6): 3346–3353, doi: 10.1121/1.402824.
4. Archie G.E. (1942), The electrical resistivity log as an aid in determining some reservoir characteristics, *Transactions of the AIME*, **146**(01): 54–62.
5. Auriault J.L., Boutin C., Geindreau C. (2010), *Homogenization of Coupled Phenomena in Heterogenous Media*, Vol. 149, John Wiley & Sons, doi: 10.1002/9780470612033.
6. Avellaneda M., Torquato S. (1991), Rigorous link between fluid permeability, electrical conductivity, and relaxation times for transport in porous media, *Physics of Fluids A: Fluid Dynamics*, **3**(11): 2529–2540, doi: 10.1063/1.858194.
7. Boutin C., Geindreau C. (2008), Estimates and bounds of dynamic permeability of granular media, *The Journal of the Acoustical Society of America*, **124**(6): 3576–3593, doi: 10.1121/1.2999050.
8. Brakke K.A. (1992), The surface evolver, *Experimental Mathematics*, **1**(2): 141–165, doi: 10.1080/10586458.1992.10504253.
9. Buffel B., Desplentere F., Bracke K., Verpoest I. (2014), Modelling open cell-foams based on the Weaire–Phelan unit cell with a minimal surface energy approach, *International Journal of Solids and Structures*, **51**(19–20): 3461–3470, doi: 10.1016/j.ijsolstr.2014.06.017.
10. Champoux Y., Allard J.F. (1991), Dynamic tortuosity and bulk modulus in air-saturated porous media, *Journal of Applied Physics*, **70**(4): 1975–1979, doi: 10.1063/1.349482.
11. Chevillotte F., Perrot C. (2017), Effect of the three-dimensional microstructure on the sound absorption of foams: A parametric study, *The Journal of the Acoustical Society of America*, **142**(2): 1130–1140, doi: 10.1121/1.4999058.
12. Costa A. (2006), Permeability-porosity relationship: A reexamination of the Kozeny-Carman equation based on a fractal pore-space geometry assumption, *Geophysical Research Letters*, **33**(2): L02318, doi: 10.1029/2005GL025134.
13. Dib L., Bouhedja S., Amrani H. (2015), Mechanical parameters effects on acoustic absorption at polymer foam, *Advances in Materials Science and Engineering*, **2015**: 896035, doi: 10.1155/2015/896035.
14. Doutres O., Atalla N., Dong K. (2011), Effect of the microstructure closed pore content on the acoustic behavior of polyurethane foams, *Journal of Applied Physics*, **110**(6): 064901, doi: 10.1063/1.3631021.
15. Doutres O., Atalla N., Dong K. (2013), A semi-phenomenological model to predict the acoustic behavior of fully and partially reticulated polyurethane foams, *Journal of Applied Physics*, **113**(5): 054901, doi: 10.1063/1.4789595.
16. Fahy F.J. (2000), *Foundations of Engineering Acoustics*, Academic Press.
17. Gao K., van Dommelen J.A.W., Geers M.G.D. (2016), Microstructure characterization and homogenization of acoustic polyurethane foams: measurements and simulations, *International Journal of Solids and Structures*, **100**: 536–546, doi: 10.1016/j.ijsolstr.2016.09.024.
18. Gasser S., Paun F., Bréchet Y. (2005), Absorptive properties of rigid porous media: application to face centered cubic sphere packing, *The Journal of the Acoustical Society of America*, **117**(4): 2090–2099, doi: 10.1121/1.1863052.
19. Ghossein E., Lévesque M. (2012), A fully automated numerical tool for a comprehensive validation of homogenization models and its application to spherical particles reinforced composites, *International Journal of Solids and Structures*, **49**(11–12): 1387–1398, doi: 10.1016/j.ijsolstr.2012.02.021.
20. Jafari M.J., Khavanin A., Ebadzadeh T., Fazlali M., Sharak M.N., Madvari R.F. (2020), Optimization of the morphological parameters of a metal foam for the highest sound absorption coefficient using local search algorithm, *Archives of Acoustics*, **45**(3): 487–497, doi: 10.24425/aoa.2020.134066.
21. Jodrey W.S., Tory E.M. (1981), Computer simulation of isotropic, homogeneous, dense random packing of equal spheres, *Powder Technology*, **30**(2): 111–118, doi: 10.1016/0032-5910(81)80003-4.
22. Jodrey W.S., Tory E.M. (1985), Computer simulation of close random packing of equal spheres, *Physical Review A*, **32**(4): 2347, doi: 10.1103/PhysRevA.32.2347.
23. Johnson D.L., Koplik J., Dashen R. (1987), Theory of dynamic permeability and tortuosity in fluid-saturated porous media, *Journal of Fluid Mechanics*, **176**(1): 379–402, doi: 10.1017/S0022112087000727.

24. Köll J., Hallström S. (2014), Generation of periodic stochastic foam models for numerical analysis, *Journal of Cellular Plastics*, **50**(1): 37–54, doi: 10.1177/0021955X13503848.
25. Kraynik A.M., Reinelt D.A., van Swol F. (2003), Structure of random monodisperse foam, *Physical Review E*, **67**(3): 031403, doi: 10.1103/PhysRevE.67.031403.
26. Kraynik A.M., Reinelt D.A., van Swol F. (2004), Structure of random foam, *Physical Review Letters*, **93**(20): 208301, doi: 10.1103/PhysRevLett.93.208301.
27. Lafarge D. (1993), Sound propagation in porous materials with a rigid structure saturated by a viscothermal fluid: Definition of geometric parameters, electromagnetic analogy, relaxation time [in French: *Propagation du son dans les matériaux poreux à structure rigide saturés par un fluide viscothermique: Définition de paramètres géométriques, analogie electromagnétique, temps de relaxation*], PhD thesis, Le Mans.
28. Lafarge D. (2009), The equivalent fluid model, [in:] *Materials and Acoustics Handbook*, M. Bruneau, C. Potel [Eds], Wiley Online Library, doi: 10.1002/9780470611609.ch6.
29. Lafarge D., Lemarinier P., Allard J.F., Tarnow V. (1997), Dynamic compressibility of air in porous structures at audible frequencies, *The Journal of the Acoustical Society of America*, **102**(4): 1995–2006, doi: 10.1121/1.419690.
30. Lai H., Gentry-Grace C., Bonilha M., Yoerkie C. (2000), Experimental characterization of materials for acoustic performance with applications, *Proceedings of InterNoise 2000*, pp. 27–30.
31. Langlois V., Kaddami A., Pitois O., Perrot C. (2020), Acoustics of monodisperse open-cell foam: An experimental and numerical parametric study, *The Journal of the Acoustical Society of America*, **148**(3): 1767–1778, doi: 10.1121/10.0001995.
32. Lee C.Y., Leamy M.J., Nadler J.H. (2009), Acoustic absorption calculation in irreducible porous media: a unified computational approach, *The Journal of the Acoustical Society of America*, **126**(4): 1862–1870, doi: 10.1121/1.3205399.
33. Matzke E.B. (1945), The three-dimensional shapes of bubbles in foams, *Proceedings of the National Academy of Sciences*, **31**(9): 281–289, doi: 10.1073/pnas.31.9.28.
34. Matzke E.B. (1946), The three-dimensional shape of bubbles in foam-an analysis of the role of surface forces in three-dimensional cell shape determination, *American Journal of Botany*, **33**(1): 58–80, doi: 10.1002/j.1537-2197.1946.tb10347.x.
35. Nguyen C. *et al.* (2022), Polydisperse solid foams: Multiscale modeling and simulations of elasto-acoustic properties including thin membrane effects, *International Journal of Solids and Structures*, **249**: 111684, doi: 10.1016/j.ijsolstr.2022.111684.
36. Okabe A., Boots B., Sugihara K., Chiu S.N. (1992), *Spatial Tessellations. Concepts and Applications of Voronoi Diagrams*, John Wiley and Sons, Inc.
37. Olny X., Panneton R. (2008), Acoustical determination of the parameters governing thermal dissipation in porous media, *The Journal of the Acoustical Society of America*, **123**(2): 814–824, doi: 10.1121/1.2828066.
38. Panneton R., Olny X. (2006), Acoustical determination of the parameters governing viscous dissipation in porous media, *The Journal of the Acoustical Society of America*, **119**(4): 2027–2040, doi: 10.1121/1.2169923.
39. Park J.H. *et al.* (2017a), Cell openness manipulation of low density polyurethane foam for efficient sound absorption, *Journal of Sound and Vibration*, **406**: 224–236, doi: 10.1016/j.jsv.2017.06.021.
40. Park J.H. *et al.* (2017b), Optimization of low frequency sound absorption by cell size control and multiscale poroacoustics modeling, *Journal of Sound and Vibration*, **397**: 17–30, doi: 10.1016/j.jsv.2017.03.004.
41. Perrot C., Chevillotte F., Panneton R. (2008), Bottom-up approach for microstructure optimization of sound absorbing materials, *The Journal of the Acoustical Society of America*, **124**(2): 940–948, doi: 10.1121/1.2945115.
42. Perrot C. *et al.* (2012), Microstructure, transport, and acoustic properties of open-cell foam samples: Experiments and three-dimensional numerical simulations, *Journal of Applied Physics*, **111**(1): 014911, doi: 10.1063/1.3673523.
43. Perrot C., Panneton R., Olny X. (2007), Periodic unit cell reconstruction of porous media: Application to open-cell aluminum foams, *Journal of Applied Physics*, **101**(11): 113538, doi: 10.1063/1.2745095.
44. Rubinstein J., Torquato S. (1988), Diffusion-controlled reactions: Mathematical formulation, variational principles, and rigorous bounds, *The Journal of Chemical Physics*, **88**(10): 6372–6380, doi: 10.1063/1.454474.
45. Trinh V.H., Guilleminot J., Perrot C. (2018), On the construction of multiscale surrogates for design optimization of acoustical materials, *Acta Acustica united with Acustica*, **104**(1): 1–4, doi: 10.3813/AAA.919139.
46. Trinh V.H., Langlois V., Guilleminot J., Perrot C., Khidas Y., Pitois O. (2019), Tuning membrane content of sound absorbing cellular foams: Fabrication, experimental evidence and multiscale numerical simulations, *Materials and Design*, **162**: 345–361, doi: 10.1016/j.matdes.2018.11.023.
47. Vu V.D., Panneton R., Gagné R. (2019), Prediction of effective properties and sound absorption of random close packings of monodisperse spherical particles: Multiscale approach, *The Journal of the Acoustical Society of America*, **145**(6): 3606–3624, doi: 10.1121/1.5111753.
48. Weaire D., Phelan R. (1994), A counter-example to Kelvin's conjecture on minimal surfaces, *Philosophical Magazine Letters*, **69**(2): 107–110, doi: 10.1080/09500839408241577.
49. Yang X., Lu T.J., Kim T. (2014), An analytical model for permeability of isotropic porous media, *Physics Letters A*, **378**(30–31): 2308–2311, doi: 10.1016/j.physleta.2014.06.002.